Dynamic Modeling and Performance Analysis for a Wire-driven Elastic Robotic Fish

Xiaocun Liao, Chao Zhou, Qianqian Zou, Jian Wang and Ben Lu

***Abstract*— The complex and continuous undulation of fishtail facilitates extraordinary underwater motion performance for natural fish. For the widely used Multi-Joint robotic fish, a lot of joints are used to simulate continuum fishtail, resulting in some challenges, e.g., the mechanism complexity, friction losses of adjacent joints, load disequilibrium and unsmooth servomotor output power. To overcome these intractable hurdles, motivated by natural fish, this letter proposes a wire-driven elastic robotic fish, which simulates fish muscle through multi-wire drive and adopts a fishlike spine design based on elastic component. Compared with the existing wire-driven robotic fish with discrete multiple-joints-spine and single-wire drive, our robotic fish not only has continuum fishtail, but also can swing with C-Shape and S-Shape owing to multi-wire coupling drive, and simulate the energy storage behavior of fish by elastic component. Further, a Lagrangian dynamic model that models a robotic fish with continuum fishtail and passive flexible joint is developed to explore the propulsive performance and validated by extensive experiments and simulations, and our robotic fish reaches the maximum swimming speed of 0.58 *m/s*, i.e., 1.04 *BL/s*. Finally, the superiority of the proposed drive mechanism in disposing of load disequilibrium and smoothing output power of servomotor, is analyzed and validated by the comparisons between a Multi-Joint robotic fish and our robotic fish.**

I. Introduction

Since the RoboTuna was developed in MIT [1], more and more researchers have become fascinated by robotic fish, which contributes to its rapid development [2], [3], [4], [5], [6], [7], [8].

The exquisite actuators can improve the stability and efficiency of robotic fish. With the considerations of this, many researchers make great efforts to explore robotic fish based on novel actuators, e.g., fluidic actuators [2], artificial muscle [3], [4], [5] etc. Cen *et al.* [3] designed a robotic fish based on macro-fiber composite (MFC) piezoelectric bimorphs and achieved the max speed of 0.31 BL/s. A soft robot based on Multiple Shape Memory Ionic Polymer-Metal Composite (MSM-IPMC) actuator was presented by Shen [4], and multiple swimming modes were obtained by controlling the artificial muscle actuators. Li *et al.* [5] developed a soft robotic fish using dielectric elastomers (DEs), which can swim in 10900-m depth underwater.

*This work was supported by National Nature Science Foundation of China (62033013, 61903362, 62003341, 61973303). (Corresponding author: Chao Zhou.)

The authors are with the State Key Laboratory of Management and Control for Complex Systems, Institute of Automation, Chinese Academy of Sciences, Beijing, 100190, China, and also with the School of Artificial Intelligence, University of Chinese Academy of Sciences, Beijing, 100049, China (e-mail:liaoxiaocun2019@ia.ac.cn; chao.zhou@ia.ac.cn; zouqianqian2019@ia.ac.cn; jianwang@ia.ac.cn; luben2019@ia.ac.cn;).

Inspired by the fact that fish in nature utilizes its muscles to drive tail [9], the wire-driven robotic fish has gradually attracted researchers' attentions. The robotic fish with active wire-driven body and compliant tail, whose maximum speed was $2.15\ BL/s$, was developed by Zhong [6]. A wire-driven robotic shark with the maximum speed of $0.22\ BL/s$, which could achieve forward motion and ascending motion by its caudal fin, was presented in [7]. Based on vector propulsion, Li *et al.* [8] designed a wire-driven robotic fish capable of two swimming modes similar to shark and dolphin. However, most of the wire-driven robotic fishes adopt discrete multiple joints to imitate fish spine, which results in some challenging troubles, such as discontinuity fishtail, the friction losses of the adjacent discrete joints etc. In addition, only the C-shape swing can be achieved due to single-wire drive. Some robotic fishes adopt multi-wire drive to obtain C-Shape swing in multiple directions instead of S-Shape [7], [8].

The dynamics of the robotic fish is a significant tool for motion control and performance optimization. Based on the Newton-Euler dynamics, Zheng *et al.* [10] developed a 3-D dynamic model of an active-tail-actuated robotic fish, which was validated by multiple 3-D motions, including surfacing motion, and spiral motion etc. Based on Lagrangian dynamics, the dynamic model for an ostraciiform robotic fish was presented by Wang [11] and angle of attack theory was taken into consideration. Using Kirchhoff's equations, Wang *et al.* [12] developed an averaging tail-actuated dynamic model of robotic fish. Currently, the successful dynamics only focus on the robotic fish with discontinuity fishtail and there are lacks of the dynamic models for robotic fish with continuum fishtail that can emulate natural fish better.

In this letter, a Wire-driven Elastic Robotic Fish (WE-Rofi), which simulates fish muscle through multi-wire drive[9] and adopts a fishlike spine design based on elastic component, is proposed. Compared with Multi-Joint robotic fish and the existing wire-driven robotic fish [6], [7], [8], the WE-Rofi not only owns continuum fishtail, but also can swing with C-shape and S-shape, and simulate the energy storage behavior of fish by elastic component [13]. Secondly, we developed a Lagrangian dynamic model that is available to robotic fish with continuum fishtail and passive flexible joint (PF-Joint) to explore the performance of WE-Rofi, and conduct extensive experiments and simulations to validate the proposed model. Thirdly, to validate the superiority of the proposed drive mechanism, the comparison experiments between a Multi-Joint robotic fish and WE-Rofi are conducted, and the results show that the WE-Rofi does better in disposing of load disequilibrium, smoothing output power of

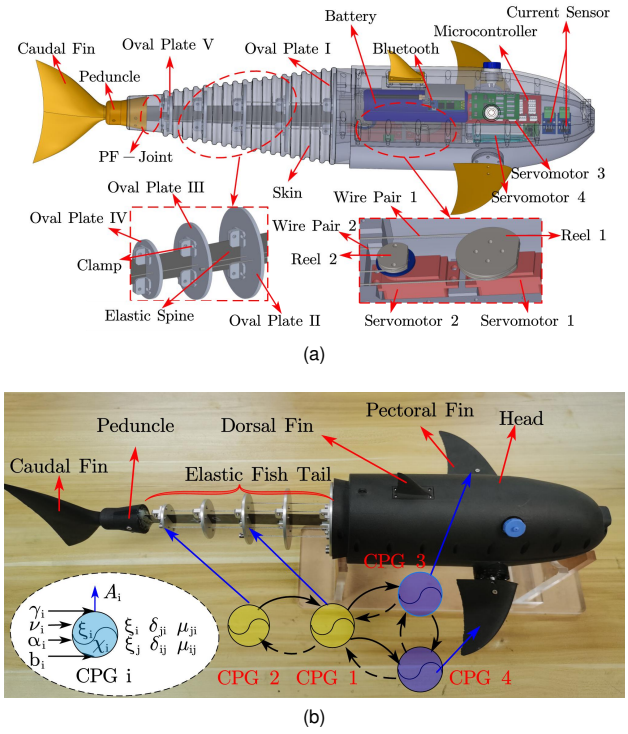

Fig. 1. Overview of the WE-Rofi. (a) Schematic design. (b) Prototype.

servomotor, and even improving propulsive efficiency.

II. Overview of the WE-Rofi

A. Mechatronic Design of the WE-Rofi

Fig. 1 shows the design of WE-Rofi, which is composed of a rigid head, a wire-driven elastic tail, a pair of pectoral fin, and a rigid caudal fin. Its size and mass are $558.5(L) \times 90(W) \times 130(H)\ mm^3$ and $2.025\ kg$, respectively. Besides, a pair of pectoral fin with two degree of freedom (DOF) are equipped to achieve 3D motion. The fish head is divided into a upper control cabin, where control circuit, battery and sensors are equipped, and a lower drive cabin, where four servomotors, two reels are mounted. Four servomotors are coordinated to obtain the fishlike motions, *e.g.*, forward motion, yaw, pitch etc. Some sensors, such as current sensor, inertial measurement unit (IMU) etc., are equipped to perceive own or external environment information.

To simulate the continuum fishtail, the elastic component, i.e., spring steel, is adopted as the fishlike elastic spine for the WE-Rofi, and holds the trapezoidal shape inspired by the convergent fish spine. The spring steel not only is low cost and easy assembly, but also is capable of large range of stiffness by slight adjustments of thickness, which is beneficial to the exploration of propulsive performance on tail-stiffness. Further, five oval metal plates I - V are sequentially installed on the elastic spine and fixed by several clamps. These five oval plates, whose sizes decrease successively, are applied to support fish skin for keeping the convergent shape of fishtail. Similar to the fish muscles [9], two wire pairs are applied to transmit the output torques of servomotor 1 and 2 to the oval plates III and V of fishtail, respectively, for achieving fishlike swing. Compared with most of existing wire-driven robotich fish, due to elastic spine and multi-wire coupling drive, our WE-Rofi not only has continuum fishtail, but also achieves C-Shape and S-Shape swing, and the fishlike energy storage behavior, which improves bionic degree highly. The tail is sealed by silicone rubber, and the caudal fin is connected to the end of the elastic spine by peduncle. In fact, the connection joint between fishtail and caudal fin can be taken as a PF-Joint, which can cause the phase delay and improve motion performance in some cases [14].

B. CPG Controller

The Ijspeert's CPG model [15] with the advantages of few parameters and explicit meaning of parameters is adopted in this letter. The Ijspeert's oscillator is as follows:

$$\begin{cases} \dot{\xi}_i = 2\pi\vartheta_i + \sum\limits_{j,j\neq i} \chi_i \delta_{ij} sin(\xi_j - \xi_i - \mu_{ij}) \\ \ddot{\chi}_i = \alpha_i(\frac{\alpha_i}{4}(\gamma_i - \chi_i) - \dot{\chi}_i) \\ A_i = \chi_i cos(\xi_i) + b_i \end{cases} \tag{1}$$

where ξ_i and χ_i are the state variables representing the phase and amplitude of the *i*-th oscillator, respectively; ϑ_i and γ_i determine convergence frequency and amplitude, respectively, and α_i that is positive constant determines the convergence speed. The coupling between the *i*-th and *j*-th oscillator is determined by the weight δ_{ij} and phase deviation μ_{ij}. b_i and A_i are the offset and final output signal of the *i*-th oscillator, respectively. As shown in Fig. 1b, a CPG network with four Ijspeert's oscillators is constructed.

III. Dynamic Modeling of the WE-Rofi

A. Coordinate System and Notations

Owing to the continuum fishtail of the WE-Rofi, some reasonable assumptions need to be made to facilitate the modeling analysis. For ease of presentation, the fishtail of oval plates I to III and III to V are referred to as the flexible link $\hat{L_1}$ and $\hat{L_2}$, respectively. Assuming that the two flexible links are all arcs after bending, named as arc assumption, and the swing amplitude of the fishtail is relatively small, $\hat{L_1}$ and $\hat{L_2}$ are approximatively taken as the corresponding chords, named as the virtual link L_1 and L_2, respectively. Since the length of the PF-Joint is much smaller than the body length, only the lag angle is taken into consideration, and the length and mass are ignored. In other words, the PF-Joint is approximatively equivalent to a torsion spring.

Then, some coordinate systems and notations are defined. As shown in Fig. 2, the inertial coordinate system $C_w = \{O_w - X_w Y_w Z_w\}$, whose plane $\{O_w X_w Y_w\}$ is fixed on the water surface, is defined. The axis Z_w is determined by the right-hand rule and points upward. Four relative coordinate systems $C_i = \{O_i - X_i Y_i Z_i\}$, $i \in [0, 3]$, which are attached to L_i, are defined. Significantly, L_0 represents the head, L_1 and L_2 represent the equivalent virtual links of $\hat{L_1}$ and $\hat{L_2}$, respectively, and L_3 represents the caudal fin. For C_i, the origin O_i is located at the starting point of L_i, i.e., the center of the *i*-th joint J_i, the axis X_i is parallel to L_i, the plane

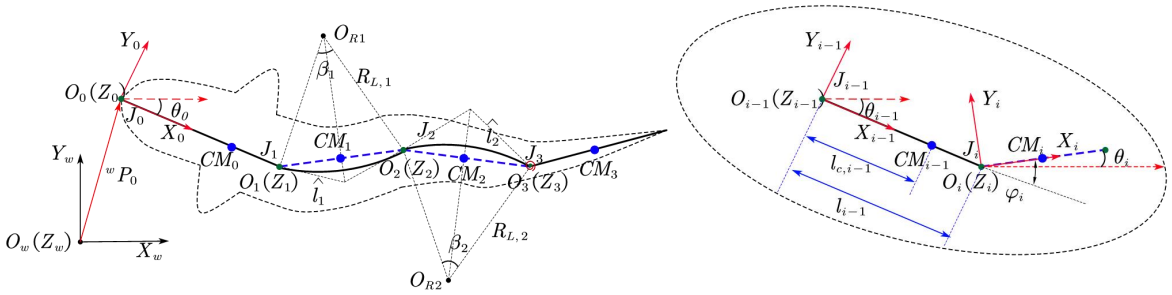

Fig. 2. The schematic illustration of coordinate system.

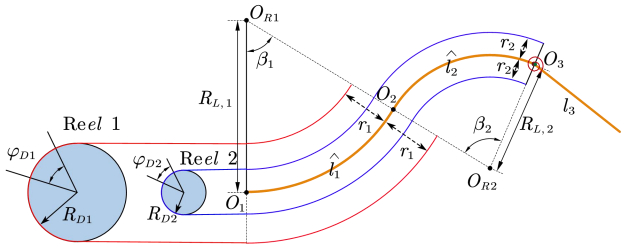

Fig. 3. The schematic diagram of the fishtail swing.

$\{O_iX_iY_i\}$ coincide with the plane $\{O_wX_wY_w\}$, and the axis Z_i is defined according to the right-hand rule.

The length and mass of L_i are defined as l_i and m_i, respectively, and the length of $\hat{L}_i$ is denoted as $\hat{l}_i$. The average height and width of L_i are denoted as h_i and w_i, respectively. The center of mass (CM) of L_i is denoted as CM_i and the length between CM_i and J_i is $l_{c,i}$. θ_i is defined as the angle between the axis X_w and X_i. The angle between L_i and L_{i-1} is defined as φ_i $(i = 1, 2, 3)$. Note that φ_i $(i = 1, 2)$ are indirectly determined by angles of two servomotors, and φ_3 is unknown due to the PF-joint J_3. All angles defined in this letter follow right-hand rule. Particularly, β_i $(i = 1, 2)$, representing the central angle of $\hat{L}_i$, are defined as positive when bending to right.

B. Kinematics Model

To establish the forward kinematics, the mechanism coupling of the WE-Rofi need to be solved firstly. As shown in Fig. 3, the changes of two wire pairs can be expressed as:

$$\begin{cases} \Delta l_1 = R_{D_1}\varphi_{D_1} = r_1\beta_1 \\ \Delta l_2 = R_{D_2}\varphi_{D_2} = r_2\beta_1 + r_2\beta_2, \end{cases} \tag{2}$$

where Δl_1 and Δl_2 are the changes for wire pair 1 and 2, respectively; R_{D_1} and R_{D_2} are radii for the 1st and 2nd reel, respectively; r_1 and r_2 are distances between wire pair 1, 2 and the body axis of fishtail, respectively; φ_{D_1} and φ_{D_2} are rotation angles of the 1st and 2nd reel and equal to A_1 and A_2 of CPG output, respectively. Then, we can obtain:

$$\beta_1 = R_{D_1}\varphi_{D_1}/r_1, \quad \beta_2 = R_{D_2}\varphi_{D_2}/r_2 - \beta_1, \tag{3}$$

$$R_{L,1} = \hat{l}_1/\beta_1, \quad R_{L,2} = \hat{l}_2/\beta_2, \tag{4}$$

$$l_1 = 2R_{L,1}sin(\beta_1/2), \quad l_2 = 2R_{L,2}sin(\beta_2/2), \tag{5}$$

where $R_{L,1}$ and $R_{L,2}$ are the arc radii of $\hat{L}_1$ and $\hat{L}_2$ after bending, respectively. Specially, if β_i $(i = 1, 2)$ is equal to zero, $R_{L,i}$ is infinite, which is a singular case. According to the Fig. 2, φ_i and θ_i can be derived.

$$\varphi_1 = \beta_1/2, \quad \varphi_2 = \beta_1/2 + \beta_2/2 \tag{6}$$

$$\theta_i = \theta_{i-1} + \varphi_i, \quad (i = 1, 2, 3) \tag{7}$$

The rotating transformation matrix of C_i with respect to C_w, i.e., ${}^wR_i$, and the position vector of O_i with respect to C_{i-1}, i.e., ${}^{i-1}P_i$, can be expressed as follows:

$${}^wR_i = \begin{bmatrix} cos\theta_i & -sin\theta_i & 0 \\ sin\theta_i & cos\theta_i & 0 \\ 0 & 0 & 1 \end{bmatrix}, \; {}^{i-1}P_i = \begin{bmatrix} l_{i-1} \\ 0 \\ 0 \end{bmatrix}. \tag{8}$$

Further, the position vector of CM_i in C_w, i.e., ${}^wr_i$, can be derived by

$${}^wr_i = {}^wR_i \, {}^ir_i + {}^wP_i, \tag{9}$$

$${}^wP_i = {}^wP_0 + \textstyle\sum_{j=1}^{i} {}^wR_{j-1} \, {}^{j-1}P_j, \tag{10}$$

where ${}^ir_i$ is the position vector of CM_i in C_i; ${}^wP_i$ is the position vector of O_i in the C_w, and ${}^wP_0 = [x_0 \; y_0 \; 0]^T$, determining the position of the WE-Rofi, is the position vector of O_0 in C_w. Apparently, the translational velocity ${}^wv_i = [{}^wv_{x,i} \; {}^wv_{y,i} \; {}^wv_{z,i}]^T$ of CM_i with respect to C_w is the differentiation of ${}^wr_i$ with respect to time t, that is,

$${}^wv_i = {}^w\dot{r}_i = {}^w\dot{R}_i \, {}^ir_i + {}^wR_i \, {}^i\dot{r}_i + {}^w\dot{P}_i, \tag{11}$$

where ${}^w\dot{R}_i = \hat{\omega}_i \, {}^wR_i$, $\hat{\omega}_i$ is the skew-symmetric matrix of ${}^w\omega_i$, and ${}^i\dot{r}_i$ is the velocity of CM_i with respect to C_i. According to the Eq. 5, the length of L_i $(i = 1, 2)$ are variable, which means that ${}^i\dot{r}_i$ are unequal to zero.

Similarly, the angular velocity can be expressed by

$$\begin{cases} {}^w\omega_0 = \begin{bmatrix} 0 & 0 & \dot{\theta}_0 \end{bmatrix}^T \\ {}^w\omega_i = {}^w\omega_{i-1} + {}^wR_i \, {}^i\omega_i, \quad (i = 1, 2, 3), \end{cases} \tag{12}$$

where ${}^w\omega_i = [{}^w\omega_{x,i} \; {}^w\omega_{y,i} \; {}^w\omega_{z,i}]^T$ and ${}^i\omega_i = [0 \; 0 \; \dot{\varphi}_i]^T$ are the angular velocity of CM_i in C_w and C_i, respectively.

C. Lagrangian Dynamics Modeling

This letter only focuses on the planar motion, and φ_3 is unknown due to the PF-joint J_3. Consequently, there are four degrees of freedom (DOF). Compared with Newtonian Euler model, Lagrangian modeling method only focuses on the system energy without the consideration of internal force, which is undoubtedly efficient for WE-Rofi due to the unknown torque of the PF-joint.

Let denote $X = x_0$, $Y = y_0$, $\Theta = \theta_0$, $\Phi = \varphi_3$. Further, the generalized coordinates and velocity can be described as $\mathbf{q} = [X\ Y\ \Theta\ \Phi]^T$ and $\dot{\mathbf{q}} = \left[\dot{X}\ \dot{Y}\ \dot{\Theta}\ \dot{\Phi}\right]^T$, respectively.

The Lagrangian function $\pounds(\mathbf{q}, \dot{\mathbf{q}}, t)$ can be expressed by

$$\pounds(\mathbf{q}, \dot{\mathbf{q}}, t) = T(\mathbf{q}, \dot{\mathbf{q}}, t) - E(\mathbf{q}, \dot{\mathbf{q}}, t), \tag{13}$$

$$T(\mathbf{q}, \dot{\mathbf{q}}, t) = \sum_{i=0}^{3} \frac{1}{2}\ {}^{w}v_i^T M_i\ {}^{w}v_i + \sum_{i=0}^{3} \frac{1}{2}\ {}^{w}\omega_i^T I_i\ {}^{w}\omega_i, \tag{14}$$

where $T(\mathbf{q}, \dot{\mathbf{q}}, t)$ and $E(\mathbf{q}, \dot{\mathbf{q}}, t)$ are kinetic energy and potential energy, respectively; M_i and I_i are the mass matrix and inertia tensor, respectively.

For $E(\mathbf{q}, \dot{\mathbf{q}}, t)$, the gravitational potential energy E_G is constant due to planar motion, and the potential energy of torsion spring $E_T(\mathbf{q}, \dot{\mathbf{q}}, t)$ should be considered. Since $\hat{L}_i$ $(i = 1, 2)$ is actively driven by two servomotors, the potential energy of $\hat{L}_i$, $E_i(\mathbf{q}, \dot{\mathbf{q}}, t)$, has no impact on $\pounds(\mathbf{q}, \dot{\mathbf{q}}, t)$. Concretely, $E_i(\mathbf{q}, \dot{\mathbf{q}}, t)$ can be derived under the assumption of pure bending, that is, the axial pressure is ignored,

$$E_i(\mathbf{q}, \dot{\mathbf{q}}, t) = T_{e,i}\beta_i/2, \quad T_{e,i} = \beta_i E I_{Z,i}/\hat{l}_i, \tag{15}$$

where $T_{e,i}$ is the bending moment of $\hat{L}_i$, E and $I_{Z,i}$ are the Elastic Modulus and the moment of inertia of an area with respect to neutral axis of the spring steel, respectively. According to Eq. 15, the $\mathbf{q}$ and $\dot{\mathbf{q}}$ are all not contained in the $E_i(\mathbf{q}, \dot{\mathbf{q}}, t)$, that is, $E_i(\mathbf{q}, \dot{\mathbf{q}}, t) = E_i(t)$, meaning that the partial derivative of $E_i(\mathbf{q}, \dot{\mathbf{q}}, t)$ with respect to $\mathbf{q}$ and $\dot{\mathbf{q}}$ are zero. As a result, the potential energy $E(\mathbf{q}, \dot{\mathbf{q}}, t)$ can be expressed as follows:

$$E(\mathbf{q}, \dot{\mathbf{q}}, t) = K_s(\varphi_3 - \beta_2/2)^2/2 + E_G, \tag{16}$$

where K_s is the spring constant of torsion spring.

Finally, the Lagrangian dynamic model is expressed by

$$\frac{d}{dt}\frac{\partial \pounds}{\partial \dot{\mathbf{q}}} - \frac{\partial \pounds}{\partial \mathbf{q}} = [F_x \quad F_y \quad T_0 \quad T_3]^T, \tag{17}$$

where the generalized forces, F_x and F_y, are the components of hydrodynamic forces on the axis X_w and Y_w, respectively, and the generalized moments, T_0 and T_3, are the moments generated by hydrodynamic forces with respect to J_0 and J_3, respectively.

D. Hydrodynamic Force Analysis

We assume that the fluid is inviscid, incompressible and irrotational, and the hydrodynamic forces acting on the WE-Rofi include the added mass forces and drag forces.

Firstly, the added mass forces of the link L_i are denoted as ${}^{w}F_{a,i} = \left[\ {}^{w}F_{ax,i}\ \ {}^{w}F_{ay,i}\ \ {}^{w}F_{az,i}\ \right]^T$, which acts on CM_i, and can be expressed in the C_w as follows:

$${}^{w}F_{a,i} = -m_{a,i}\left[\ {}^{w}\dot{v}_{x,i}\ {}^{w}\dot{v}_{y,i}\ 0\ \right]^T, \tag{18}$$

where $m_{a,i}$ is the added mass, and equal to the product of the mass m_i and the added mass coefficient $c_{m,i}$; ${}^{w}\dot{v}_{x,i}$ and ${}^{w}\dot{v}_{y,i}$ are the components of the acceleration of CM_i on the axis X_w and Y_w, respectively.

Secondly, the drag forces of the link L_i, which also acts on the CM_i hypothetically, is described in the C_i by

$${}^{i}F_{d,i} = \begin{bmatrix} {}^{i}F_{dx,i} \\ {}^{i}F_{dy,i} \\ {}^{i}F_{dz,i} \end{bmatrix} = \begin{bmatrix} -\frac{1}{2}c_{f,i}\rho S_{x,i}|{}^{i}v_{x,i}|{}^{i}v_{x,i} \\ -\frac{1}{2}c_{d,i}\rho S_{y,i}|{}^{i}v_{y,i}|{}^{i}v_{y,i} \\ 0 \end{bmatrix} \tag{19}$$

where $c_{f,i}$ and $c_{d,i}$ are the friction coefficient and drag coefficient of L_i, respectively; $S_{x,i}$ and $S_{y,i}$ represent the characteristic areas of L_i with respect to the axis X_i and Y_i, respectively; ρ is the fluid density; ${}^{i}v_{x,i}$ and ${}^{i}v_{y,i}$ represent the translational velocity of CM_i in the C_i, respectively. The drag forces are expressed in the C_w as follows.

$${}^{w}F_{d,i} = \left[\ {}^{w}F_{dx,i}\ {}^{w}F_{dy,i}\ {}^{w}F_{dz,i}\ \right]^T = {}^{w}R_i\ {}^{i}F_{d,i} \tag{20}$$

Finally, we can obtain the generalized forces and moments.

$$\begin{cases} F_x = \sum_{i=0}^{3} {}^{w}F_{ax,i} + \sum_{i=0}^{3} {}^{w}F_{dx,i} \\ F_y = \sum_{i=0}^{3} {}^{w}F_{ay,i} + \sum_{i=0}^{3} {}^{w}F_{dy,i} \\ T_0 = \sum_{i=0}^{3} {}^{w}\tau_{a0,i} + \sum_{i=0}^{3} {}^{w}\tau_{d0,i} \\ T_3 = \sum_{i=0}^{3} {}^{w}\tau_{a3,i} + \sum_{i=0}^{3} {}^{w}\tau_{d3,i} \end{cases} \tag{21}$$

where ${}^{w}\tau_{a0,i}$ and ${}^{w}\tau_{d0,i}$, representing the moments of J_0, are generated from added mass forces and drag forces in the C_w, respectively. Similarly, ${}^{w}\tau_{a3,i}$ and ${}^{w}\tau_{d3,i}$ are for J_3.

IV. Simulations and Experiments

A. Experimental Platform

The experiments are carried out in a pool of 5 m long and 4 m wide. A global camera, which can capture the motion of the WE-Rofi, is hung over the pool. Besides, the target tracking algorithm, based on Kernel Correlation Filter (KCF), is applied to extract the positions of the WE-Rofi.

B. Validation of Dynamic Model

Due to the complexity of the interactions between robotic fish and fluid, the hydrodynamic parameters are difficult to determine. In this letter, the nonlinear optimization expressed by Eq. 22 is applied to identify the hydrodynamic parameters.

$$\min_{\lambda} f = \min_{\lambda} \sum_{i=1}^{m} \int_0^t |v_{e,i}(t) - v_{s,i}(t)|dt \tag{22}$$

$v_{e,i}$ and $v_{s,i}$ represent the resultant velocity of experiment and simulation under the frequency f_i, respectively, and λ is the collection of hydrodynamic parameter, including $c_{m,i}$, $c_{f,i}$ and $c_{d,i}$ $(i = 0 - 3)$. In this letter, the velocity of

TABLE I

THE VALUES OF PARAMETERS OF CPG 1 AND 2

Parameter	ϑ_{1-2}	δ_{12}	δ_{21}	μ_{12}
Unit	Hz	- [a]	-	rad
Value	1+0.25*k, k=0-8	-0.41	0.64	1.76
Parameter	μ_{21}	γ_1	γ_2	α_{1-2}	b_{1-2}
Unit	rad	rad	rad	-	rad
Value	1.06	0.66	0.57	20	0

[a] "–" denotes dimensionless.

TABLE II

THE PHYSICAL PARAMETERS OF THE WE-ROFI

Name	L_0	$\hat{L_1}$	$\hat{L_2}$	L_3	Unit
m_i	2.2842	0.0750	0.0393	0.0615	kg
l_i	0.2630	0.0800	0.0800	0.1355	m
h_i	0.1300	0.0840	0.0540	0.0400	m
w_i	0.0900	0.0640	0.0420	0.0320	m
$l_{c,i}$	0.1315	0.0400	0.0400	0.0677	m
$S_{x,i}$	117.00	53.76	22.68	12.80	cm^2
$S_{y,i}$	342.00	67.20	43.20	53.40	cm^2

the central position of the color block on head represents the velocity of WE-Rofi. In particular, due to the structural complexity of the PF-Joint, the spring constant K_s is also identified. For simplicity, $c_{m,i}$ for all links are assumed to be equal. Due to the similar structures and materials for the flexible link $\hat{L_1}$ and $\hat{L_2}$, the same friction coefficient $c_{f,i}$ and drag coefficient $c_{d,i}$ are be set, respectively [14]. The data with the different frequency f_i, and same amplitude of $8.5\ cm$, are applied to parameters identification. In this letter, just the parameters for CPG 1 and 2 are taken into account and listed in table I, and the physical parameters of the WE-Rofi are presented in table II. All physical parameters applied to simulations are measured directly or calculated indirectly. Note that we ignore the discrepancy caused by non-constant height and width of WE-Rofi in this letter.

The lower bound λ_{min}, upper bound λ_{max} and initial value λ_0 of identified parameters are chosen according to the empirical value. The identified value λ^* are tabulated in table III. Significantly, the average error of the resultant velocity for all identified data is 8.42%. Fig. 4a and 4b depict the comparisons of the resultant velocity and trajectory for the WE-Rofi with the frequency f_i of $2Hz$ and the amplitude of $8.5cm$, respectively, where the simulation time step size is $1/300$ s. The oscillation of speed is attributed to the periodic vibration existing in the head. Note that the data for parameters identification are collected from straight motions. To further validate the generalization ability of dynamic model, the comparison of turning motion with the CPG bias b_{1-2} of $0.47\ rad$ is performed. From Fig. 5, the experimental resultant velocity and trajectory match well with simulation. The average resultant speed of simulation and experiment are $0.2905m/s$ and $0.2916m/s$, respectively, and the error of average resultant speed is 0.36%. Compared with straight motion, the oscillation of speed during turning motion is more violent, which is attributed to the existences of yaw and periodic vibration of head. All of the simulation and

TABLE III

THE HYDRODYNAMIC PARAMETERS λ FOR IDENTIFICATION.

	λ_{min}	λ_{max}	λ_0	λ^*
$c_{m,0-3}$	0.01	10	0.1	0.0100
$c_{f,0}$	0.01	1.0	0.1	0.0123
$c_{f,1-2}$	0.01	1.0	0.1	0.5949
$c_{f,3}$	0.01	1.0	0.1	1.0000
$c_{d,0}$	0.01	10	1.28	2.1413
$c_{d,1-2}$	0.01	10	1.28	10.00
$c_{d,3}$	0.01	10	1.28	0.7232
K_s	0.01	5.0	1.0	1.5867

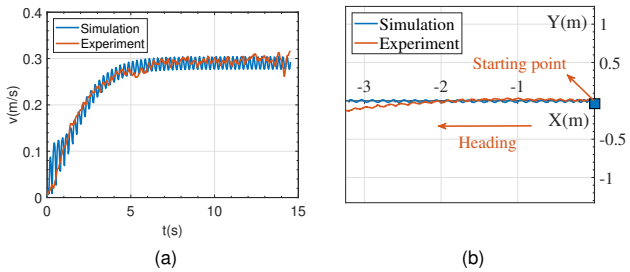

Fig. 4. The straight motion with the frequency of $2Hz$ and the amplitude of $8.5cm$. (a) The resultant speed. (b) The trajectory.

experimental data used in the validation have not been used in identifying the hydrodynamic parameters, which provides strong support for the effectiveness of dynamic model. Fig. 6 shows the snapshots of turning motion for WE-Rofi.

C. Speed Exploration

Further, the relationships between the swing frequency, amplitude, and stable swimming speed of the WE-Rofi are explored. The stable swimming speed of simulations and experiments are depicted in Fig. 7a and 7b, from which we find that the simulations agree well with experiments. Besides, the average errors of the resultant velocity for different amplitudes are tabulated in table IV, and the average error for all data is 16.1%, which signifies the generalization ability of the identified dynamic model. For swimming performance, the conclusion, the higher the frequency and amplitude of the WE-Rofi are, the greater the speed is, can be drawn according to Fig. 7. Besides, when the frequency and amplitude are $5\ Hz$ and $9\ cm$, respectively, the maximum swimming speed of $0.58\ m/s$, i.e., $1.04\ BL/s$, is obtained. The speed comparisons between our robot fish and the existing wire-driven robot fishes are presented in Table V, from which, we find that the maximum swimming speed of most of existing wire-driven robot fishes are less than $1\ BL/s$, and our WE-Rofi obtains a relatively high swimming speed of $1.04\ BL/s$.

As a widely used indicator of performance, swimming number (Sw) is expressed by $Sw = U/fL$ [17], where U is swimming speed, f and L are the swing frequency and body length, respectively. For fish, Sw is about 0.6, which indicates high performance [17]. From Fig. 8, Sw also increases with the increase of amplitude, and the maximum experimental Sw is about 0.34, when the frequency and amplitude are $1\ Hz$ and $9\ cm$, respectively. To our best knowledges, except for Zhong's robotic fish (0.72) [6], the

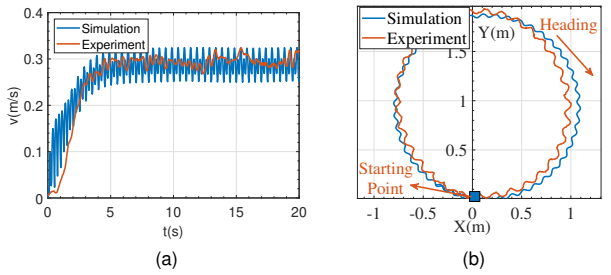

Fig. 5. The turning motion with the frequency of $2Hz$, the amplitude of $8.5cm$ and the bias of $0.47rad$. (a) The resultant speed. (b) The trajectory.

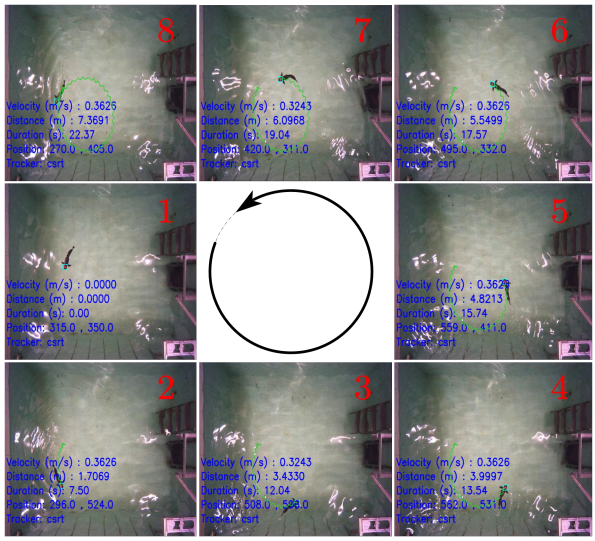

Fig. 6. The snapshot sequences of turning motion for the WE-Rofi. The green curves and blue rectangular boxes indicate the actual trajectories and detected positions of the WE-Rofi, respectively.

Sw of most of existing wire-driven robot fishes are less than 0.3, such as, Lau's (0.11) [7] and Liu's (0.176) [16], and our WE-Rofi with Sw of 0.34 are better.

D. Conclusions for Experiments

Based on the experiments and discussions above, the conclusions can be drawn as follows:

- The experimental results show that the error of average resultant speed for turning motion is 0.36% and the experimental trajectory also matches well with the simulations, which validates the proposed dynamic model.
- For WE-Rofi, the swimming speed is improved with the increases of the swing frequency and amplitude.
- Our WE-Rofi achieves the maximum swimming speed of about $0.58\ m/s$, i.e., $1.04\ BL/s$.

V. The Comparisons Between WE-Rofi and Multi-Joint Robotic Fish

As mentioned above, the potential energy of $\hat{L}_i$ $(i = 1, 2)$, $E_i(t)$, has no impact on $\pounds(\mathbf{q}, \dot{\mathbf{q}}, t)$. Consequently, it's desirable to explore the functions of the elastic component in conjunction with wire-driven mode. In this letter, we compare the power of servomotors between the WE-Rofi and

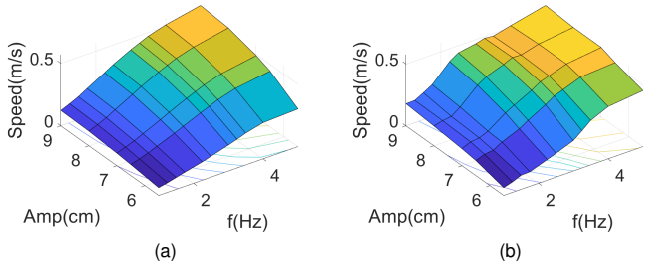

Fig. 7. The (a) simulation and (b) experimental curve of steady swimming speed, frequency and amplitude. Note that the intersection points of grid-line represent the experimental data in (b).

TABLE IV
The Average Errors for Different Amplitudes.

Amp(cm)	5.5	6.5	7.0	8.0	9.0	Average
Errors($\%$)	17.3	19.1	17.8	13.3	13.1	16.1

a Multi-Joint robotic fish, named as RobotShark and shown in Fig. 9. It's noteworthy that the RobotShark, whose size is $650(L) \times 120(W) \times 140(H)\ mm^3$ and mass is $2.498\ kg$, owns the similar sizes with WE-Rofi. In addition, we adopt the same servomotors and set the same swing frequencies and amplitudes for both robotic fish. For a better contrast with the WE-Rofi, two representative servomotors of the RobotShark, that is, the first and last servomotors, swing periodically, and the remaining servomotors keep still.

Fig. 10 depicts the change curves of power and angle of two servomotors for the RobotShark and WE-Rofi, where the swing frequency is $1\ Hz$. It should be noted that A_i represents the angle of the i-th servomotor, and the $P_{M,i}$ and $P_{W,i}$ represent the power of the i-th servomotor for the RobotShark and the WE-Rofi, respectively. From Fig. 10, we can find two advantages of the WE-Rofi.

(1) The loads of all servomotors can be balanced, which benefits from wire-driven mode.

For the RobotShark, the average of $P_{M,1}$, $8.88W$, is obviously greater than $P_{M,4}$, $2.99W$. The reason for this phenomenon of the load disequilibrium of multiple servomotors is that, for the series structure, e.g., Multi-Joint robotic fish, the i-th servomotor need to drive all posterior loads, including the links, servomotors and caudal fin. That is, the more close to the fish head the servomotor is, the bigger the load of which is. As a result, the loads of multiple servomotors vary greatly for this kind of series structure. With the increase of the number of joint, this issue will be a intractable hurdle.

Nevertheless, this phenomenon of load disequilibrium won't appear in the WE-Rofi, which benefits from the wire-driven mode. In WE-Rofi, the driving forces of fishtail are generated in head and transmitted by two wire pairs, which is the biggest difference from series structure. Compared with RobotShark, the load of two servomotors for WE-Rofi vary slightly. From Fig. 10b, the average of $P_{W,1}$ and $P_{W,2}$ are $2.72W$ and $2.36W$, respectively, and aren't much difference.

TABLE V

THE COMPARISONS WITH EXISTING WIRE-DRIVEN ROBOTIC FISH.

Robotic fish	Max Speed (BL/s)	Body Length (mm)
Lau's[7]	0.22	600
Li's[8]	0.35	425
Liu's[16]	0.44	817
Zhong's[6]	2.15	310
ours	1.04	558.5

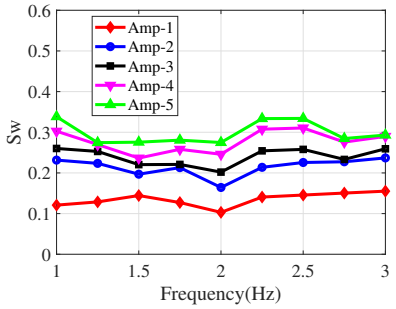

Fig. 8. The experimental Sw under different Amplitudes. $Amp-i(i=1-5)$ represent the amplitudes of $\{5.5, 6.5, 7, 8, 9\}$ cm, respectively.

Actually, force generation for some fishes is concentrated in anterior parts of the body, while posterior parts are applied to simply transmit the forces [9], [18]. This mystery of fish body is significant for robot design, for example, the WE-Rofi, to balance the loads of all servomotors.

(2) The output power of every servomotor can be smoothed, which benefits from elastic component.

For ease of presentation, the swing cycle is divided into two kinds of strokes, i.e., drive stroke, where the fishtail moves from the middle to the sides, and recovery stroke, where the fishtail moves reversely. As shown in Fig. 11, taking the last joint of RobotShark as an example, the angular acceleration of the caudal fin $\dot{\omega}'$ points to the center position of the body axis at any time, when the angle of caudal fin is sinusoidal. The directions of the angular acceleration $\dot{\omega}'$ and the hydrodynamic force F' are identical during the drive stroke, while inverse during the recovery stroke, which results in smaller servomotor torque in drive stroke than recovery stroke. Namely, the output power of the servomotor is oscillating and unsmooth in one cycle. In this letter, the peak-to-peak (PTP) value of power, which is defined as the difference between the maximum and minimum power, is applied to judge the smoothness of power of servomotor. From Fig. 10a, the PTP value of power of two servomotors for the RobotShark are $8.07W$ and $3.62W$, respectively, and relatively large. This phenomenon of unsmooth output power limits greatly the performance and reduces serviceable life of servomotor, which is a challenge for series structures.

However, the power of servomotor for the WE-Rofi is smoother than the RobotShark, which benefits from the elastic spine. The elastic spine can store energy during the drive stroke, and release the stored energy during the recovery stroke. The stored energy of elastic component is provided by servomotor, which indicates that the power of servomotor

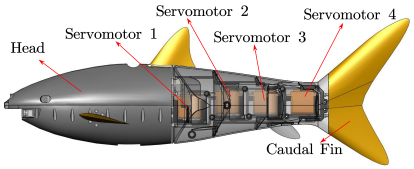

Fig. 9. Overview design of the RobotShark.

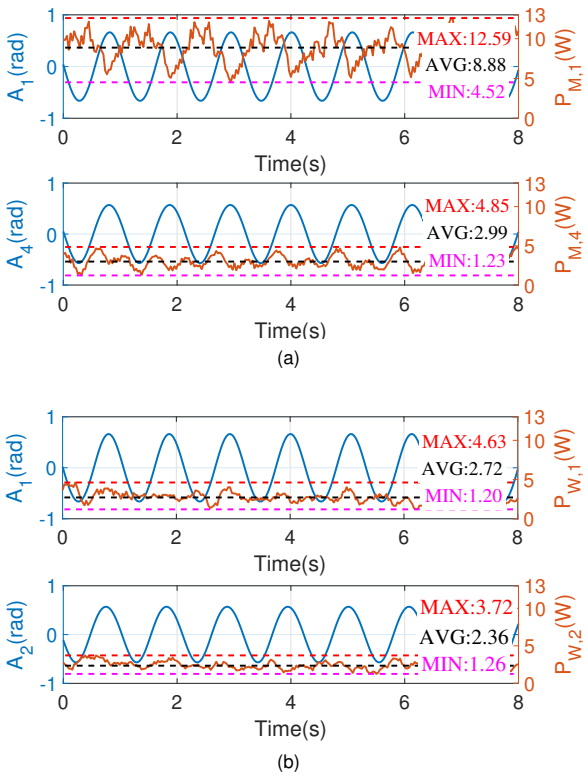

Fig. 10. The curves of power and angle of (a) the RobotShark and (b) WE-Rofi. The control frequency and sensing frequency are 50Hz.

will increase during the drive stroke. On the contrary, the power of servomotor will decrease significantly during the recovery stroke owing to the release of the stored energy. Due to the periodical energy storage and release, the output power of servomotor can be smoothed. Consequently, we can find that the PTP value of power of two servomotors for the WE-Rofi are $3.43W$ and $2.46W$, respectively, and smaller than the RobotShark, which suggests that the novel driven mechanism of the WE-Rofi can make the output power more sooth. In other words, the WE-Rofi can obtain higher average power of servomotor than RobotShark without the damage of the servomotor, and we can maximize the performance of the servomotor. Beside, some studies report that some fishes can store and release energy periodically to minimize energy consumption [13], [18]. In WE-Rofi, the PF-Joint can realize passive fishlike energy storage and release behaviors.

To analyze the propulsive efficiency, the swimming speed (U) and cost of transport (COT) defined as the ratio of the consumed power (P) to U [19], i.e., COT =P/U, are adopted. From Fig. 12a, the maximum speed of RobotShark

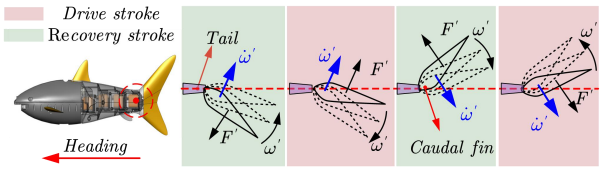

Fig. 11. The diagram of forces analysis in one cycle.

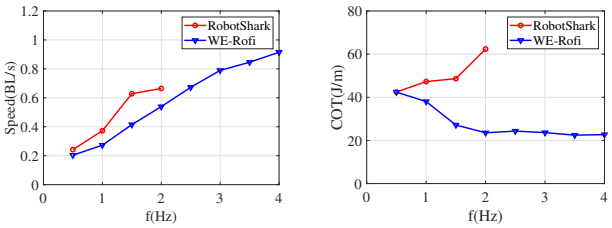

Fig. 12. The comparisons of (a) speed and (b) COT.

is 0.66 BL/s when frequency is 2 Hz, and the frequency can't be increased due to load disequilibrium and unsmooth output power. Particularly, owing to the increasing of frequency and heavy load, the servomotor 1 of RobotShark may reaches the maximum permissible power. However, the WE-Rofi is capable of the higher frequency of 4 Hz and maximum speed of 0.91 BL/s at the same amplitude, which is beneficial from the combination of wire-driven mode and elastic component. The gap in speed between RobotShark and WE-Rofi is relatively slight at same frequency, while the COT demonstrates the opposite trend according to Fig. 12b. Compared with RobotShark, the COT of WE-Rofi decreases with the increases of frequency, implying the improvements of propulsive efficiency.

VI. Conclusion and Future Work

This letter presents a wire-driven elastic robotic fish, which simulates fish muscle through multi-wire drive and adopts a fishlike spine design based on elastic components. Remarkably, due to the combinations of wire-driven mode and elastic component, our robotic fish not only owns continuous fishlike undulation, but also has the advantages of balancing the loads of all servomotors and smoothing the power of every servomotor, which don't exist in the series structure, e.g., Multi-Joint robotic fish. Then, the Lagrangian dynamic model is developed and the hydrodynamic parameters are identified. Extensive simulations and experiments validate the effectiveness of the proposed dynamic model of the WE-Rofi, which can provide a significant tool for the performance optimization and control method researches. More importantly, our WE-Rofi reaches the maximum swimming speed of 0.58 m/s, i.e., 1.04 BL/s, which is better than most of existing wire-driven robot fishes.

In the future, we will make efforts in the 3D dynamic modeling and the effect of the elastic spine on the motion performance of the WE-Rofi. In addition, the model-based control, e.g., model predictive control, also need to be done for improving the actual motion ability of the WE-Rofi.

References

[1] M. S. Triantafyllou, and G. S. Triantafyllou, "An efficient swimming machine," *Scientific American*, vol. 272, no. 3, pp. 64-70, Mar. 1995.

[2] A. D. Marchese, C. D. Onal, and D. Rus, "Autonomous soft robotic fish capable of escape maneuvers using fluidic elastomer actuators," *Soft robotics*, vol. 1, no. 1, pp. 75-87, Feb. 2014.

[3] L. Cen, and A. Erturk, "Bio-inspired aquatic robotics by untethered piezohydroelastic actuation," *Bioinspiration & biomimetics*, vol. 8, no. 1, pp. 016006, Jan. 2013.

[4] Q. Shen, Z. Olsen, T. Stalbaum, S. Trabia, J. Lee, R. Hunt, K. Kim, J. Kim and I. K. Oh, "Basic design of a biomimetic underwater soft robot with switchable swimming modes and programmable artificial muscles," *Smart Materials and Structures*, vol. 29, no. 3, pp. 035038, Feb. 2020.

[5] G. Li, X. Chen, F. Zhou, Y. Liang, Y. Xiao, X. Cao, and W. Yang, "Self-powered soft robot in the Mariana Trench," *Nature*, vol. 591, no. 7848, pp. 66-71, Mar. 2021.

[6] Y. Zhong, Z. Li, and R. X. Du, "A novel robot fish with wire-driven active body and compliant tail," *IEEE/ASME Transactions on Mechatronics*, vol. 22, no. 4, pp. 1633-1643, Jun. 2021.

[7] W. P. Lau, Y. Zhong, R. X. Du, and Z. Li, "Bladderless swaying wire-driven robot shark," *in Pro. IEEE 7th International Conference on Cybernetics and Intelligent Systems (CIS) and IEEE Conference on Robotics, Automation and Mechatronics (RAM)*, Siem Reap, Cambodia, 2015, pp. 155-160.

[8] Z. Li, Y. Zhong, and R. X. Du, "A novel underactuated wire-driven robot fish with vector propulsion," *in Proc. IEEE/RSJ International Conference on Intelligent Robots and Systems*, Tokyo, Japan, 2013, pp. 941-946.

[9] M. H. Dickinson, C. T. Farley, R. J. Full, M. A. R. Koehl, R. Kram, and S. Lehman, "How Animals Move: An Integrative View," *Science*, vol. 288, no. 5463, pp. 100-106, Apr. 2000.

[10] X. Zheng, M. Xiong, R. Tian, J. Zheng, M. Wang, and G. Xie, "Three-Dimensional Dynamic Modeling and Motion Analysis of a Fin-Actuated Robot," *IEEE/ASME Transactions on Mechatronics*, pp. 1-8, Jun. 2022.

[11] W. Wang, G. Xie, and H. Shi, "Dynamic modeling of an ostraciiform robotic fish based on angle of attack theory," *2014 International Joint Conference on Neural Networks (IJCNN). IEEE*, Beijing, China, 2014, pp. 3944-3949.

[12] J. Wang, and X. Tan, "Averaging tail-actuated robotic fish dynamics through force and moment scaling," *IEEE Transactions on Robotics*, vol. 31, no. 4, pp. 906-917, Jun. 2015.

[13] B. K. Ahlborn, *Zoological physics: Quantitative models of body design, actions, and physical limitations of animals.* Berlin Heidelberg, Germany :Springer Science & Business Media, 2006, pp. 191-230.

[14] D. Chen, Z. Wu, H. Dong, M. Tan, and J. Yu, "Exploration of swimming performance for a biomimetic multi-joint robotic fish with a compliant passive joint," *Bioinspiration & Biomimetics*, vol. 16, no. 2, pp. 026007, Dec. 2020.

[15] A. Ijspeert, A. Crespi, D. Ryczko, and J. M. CabelguenJ, "From swimming to walking with a salamander robot driven by a spinal cord model" *Science*, vol. 315, no. 5817, pp. 1416-1420, Mar. 2007.

[16] J. Liu, C. Zhang, Z. Liu, R. Zhao, D. An, Y. Wei, Z. Wu, and J. Yu, "Design and analysis of a novel tendon-driven continuum robotic dolphin," *Bioinspir.Biomim.*, vol. 16, no. 6, pp. 065002, Sep. 2021.

[17] W. Zhao, A. Ming, and M. Shimojo "Development of high-performance soft robotic fish by numerical coupling analysis," *Applied Bionics and Biomechanics*, vol. 2018, Nov. 2018.

[18] P. Valdivia y Alvarado, and K. Youcef-Toumi, "Design of machines with compliant bodies for biomimetic locomotion in liquid environments" *ASME. J. Dyn. Sys., Meas., Control.*, vol. 128, no. 1, pp. 3-13, Mar. 2006.

[19] J. Zhu, C. H. White, D. K. Wainwright, V. Di Santo, G. V. Lauder, and H. Bart-Smith, "Tuna robotics: A high-frequency experimental platform exploring the performance space of swimming fishes," *Sci. Robot.*, vol. 4, no. 34, 2019, Art. no. eaax4615.